Supplemental Material

Naoki Tsunoda[1], Yu Kumagai[2,3], Akira Takahashi[1], and Fumiyasu Oba[1,2,4]

[1]Laboratory for Materials and Structures, Institute of Innovative Research, Tokyo Institute of Technology, Yokohama 226-8503, Japan
[2]Materials Research Center for Element Strategy, Tokyo Institute of Technology, Yokohama 226-8503, Japan
[3]PRESTO, Japan Science and Technology Agency, Tokyo 113-8656, Japan
[4]Center for Materials Research by Information Integration, Research and Services Division of Materials Data and Integrated System, National Institute for Materials Science, Tsukuba 305-0047, Japan.

May 28, 2018

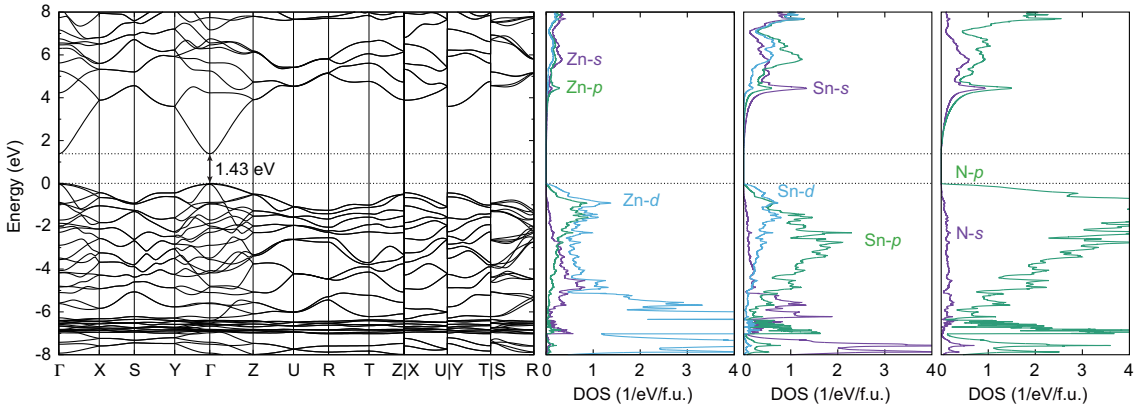

Figure S1: Band structure diagram and orbital-projected density of states (DOS) at each atomic site for the ordered orthorhombic $ZnSnN_2$ obtained using HSE06 at its theoretical lattice constants. The band path is based on Ref. [1]. The energy zero is set at the VBM. Note that the DOS near the CBM is significantly small owing to the large band dispersion.

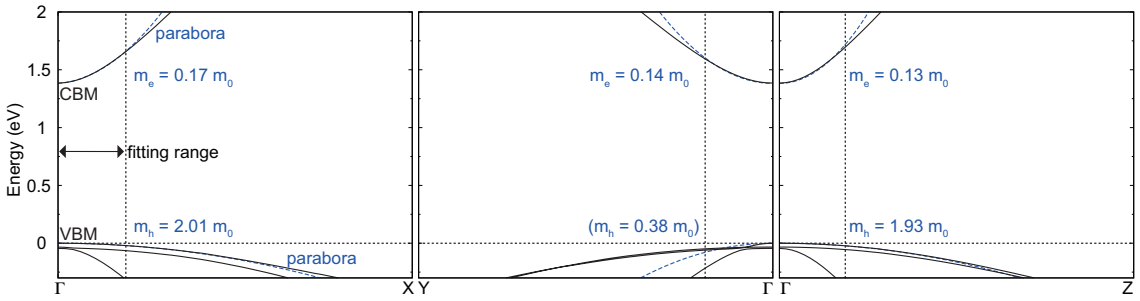

Figure S2: Electron (m_e) and heavy-hole (m_h) effective masses calculated through parabola fitting along the Γ-X, Γ-Y, and Γ-Z directions. The fitting range and the derived curves are also shown by dashed lines. The hole effective mass calculated from the split-off-like band is given in the parentheses as it does not significantly affect the averaged effective mass. These electron and heavy-hole effective masses are comparable or even superior to those of GaN (m_e =0.18m_0 and m_h = 1.97m_0 [2]).

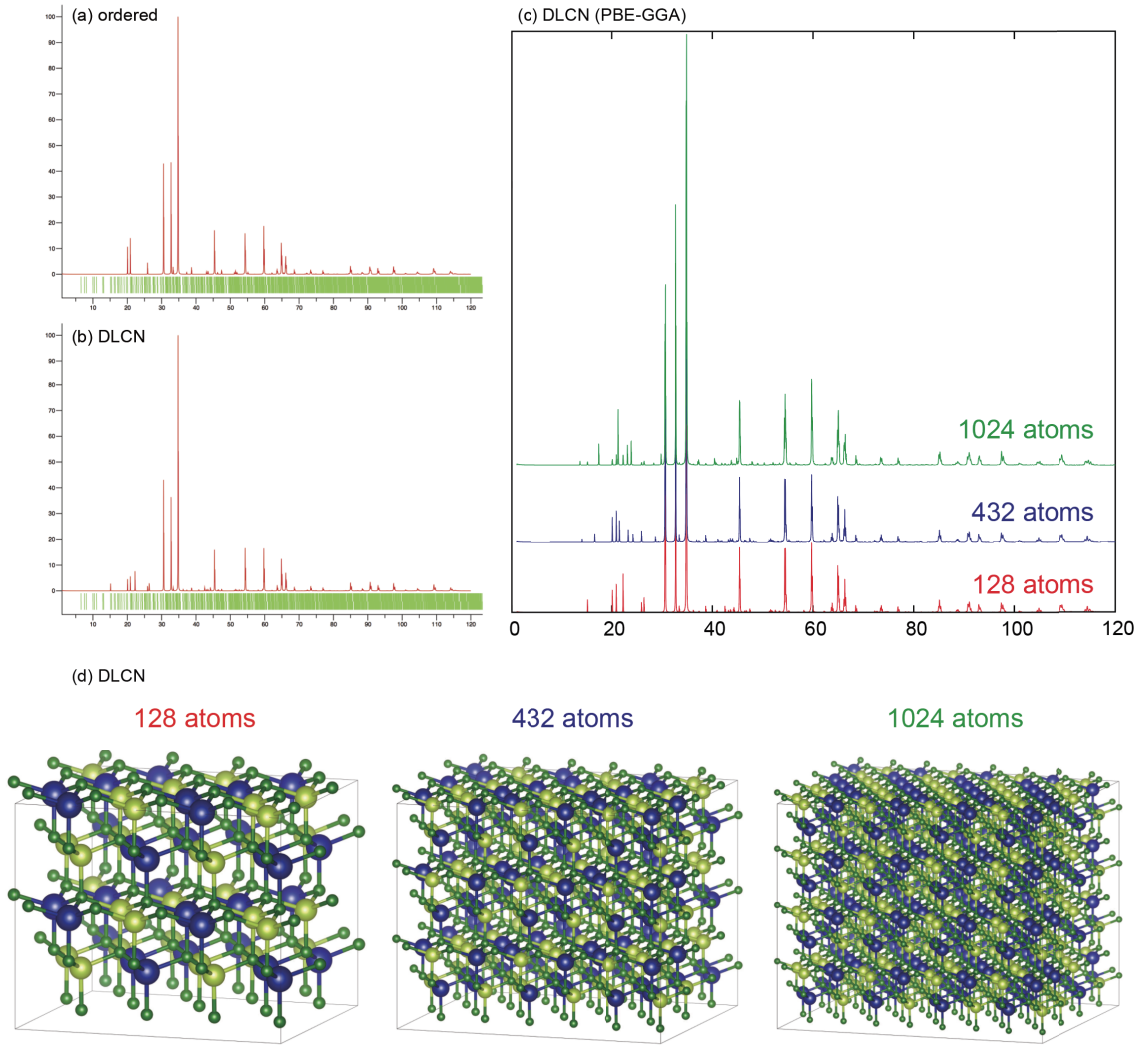

Figure S3: Simulated powder diffraction patterns for (a) the ordered structure and (b) 128-atom disordered structure with local charge neutrality (DLCN) based on the HSE06 structures. The VESTA code [3] was used in the simulations. (c) Those for the DLCN models in different cell sizes optimized using PBEsol-GGA. The supercells used for (c) are shown in (d). Note that low angle peaks vary relatively largely depending on the configurations.

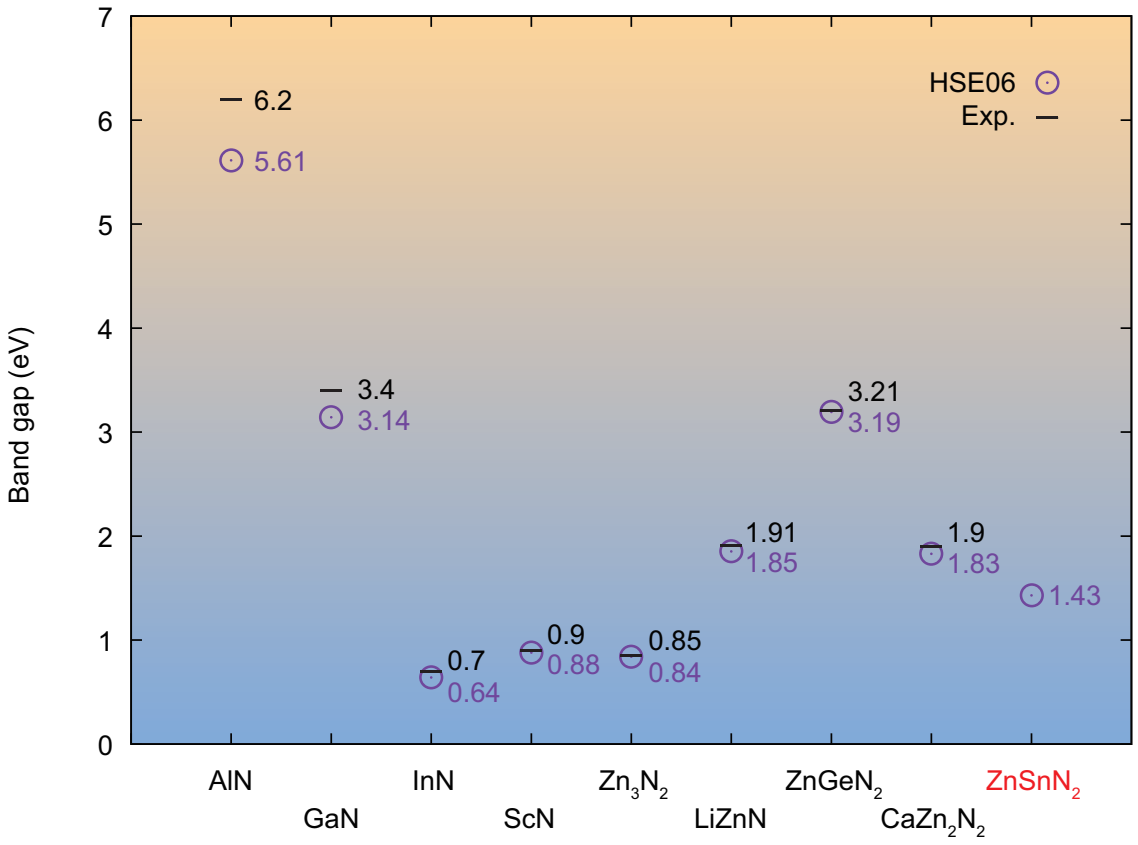

Figure S4: Experimental and HSE06 calculated band gaps of metal nitrides. Calculated values are denoted with circles and experimental values are shown with horizontal bars (see Refs. [4, 5, 6, 7, 8, 2]). The HSE06 functional accurately reproduces the band gaps up to ~ 2 eV. Note that the BM shifts have been observed in InN, Zn_3N_2, and ScN, which lead to larger optical band gaps than the fundamental direct gaps. Thus, we show the smallest experimental values among those reported.

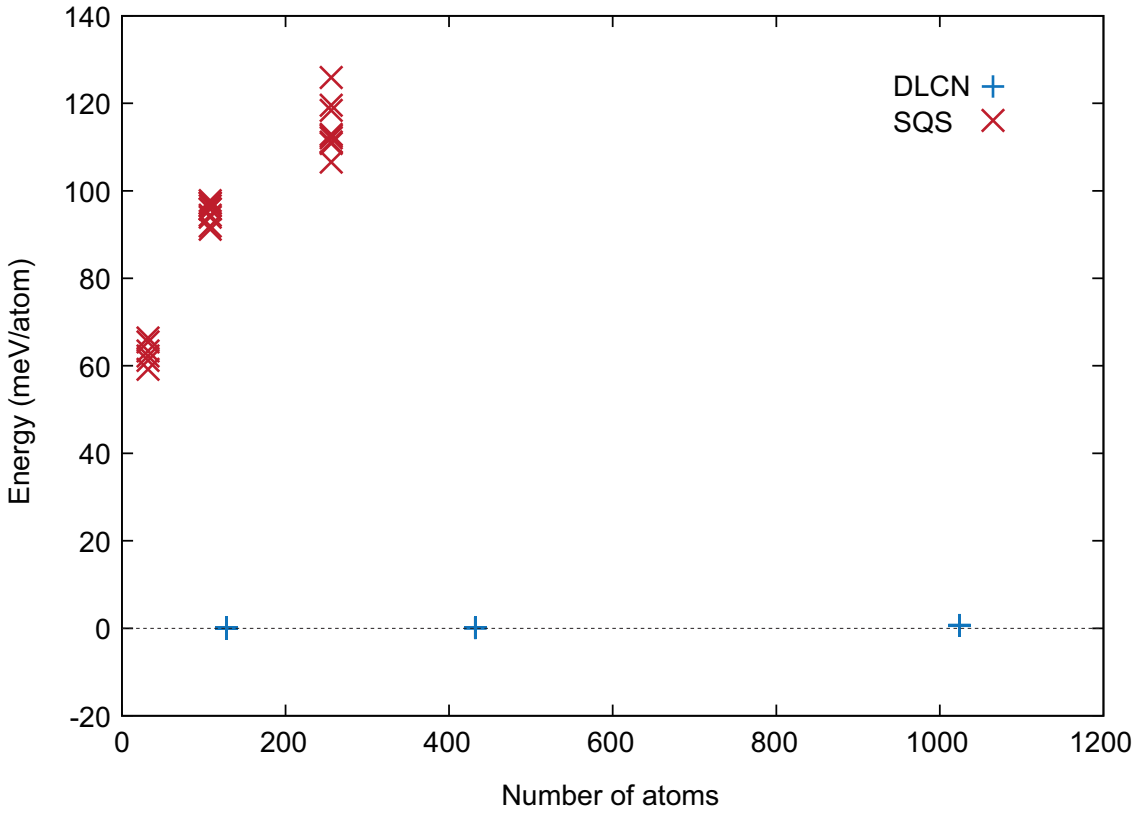

Figure S5: Relative total energies of special quasi-random structure (SQS) and DLCN models of $ZnSnN_2$ with different supercell sizes calculated using PBEsol-GGA. The energy zero is set to that of the ordered structure. The horizontal axis means the number of atoms in the supercells. Both DLCN and SQS models were generated by Monte Carlo simulated annealing (MCSA) using in-house and CLUPAN codes [9], respectively. The SQS models were obtained by optimizing the correlation functions of pairs up to the 50th nearest neighbors to mimic the fully disordered state. To check the validity of the MCSA, we repeated the search of the SQS models ten times for each supercell. Lattice relaxation was allowed for all the structures. The energy differences indicate that the DLCN models have large advantages in energy than the SQS models with fully random cation disordering; the energies of the DLCN models differ by less than 1 meV/atom from that of the ordered model.

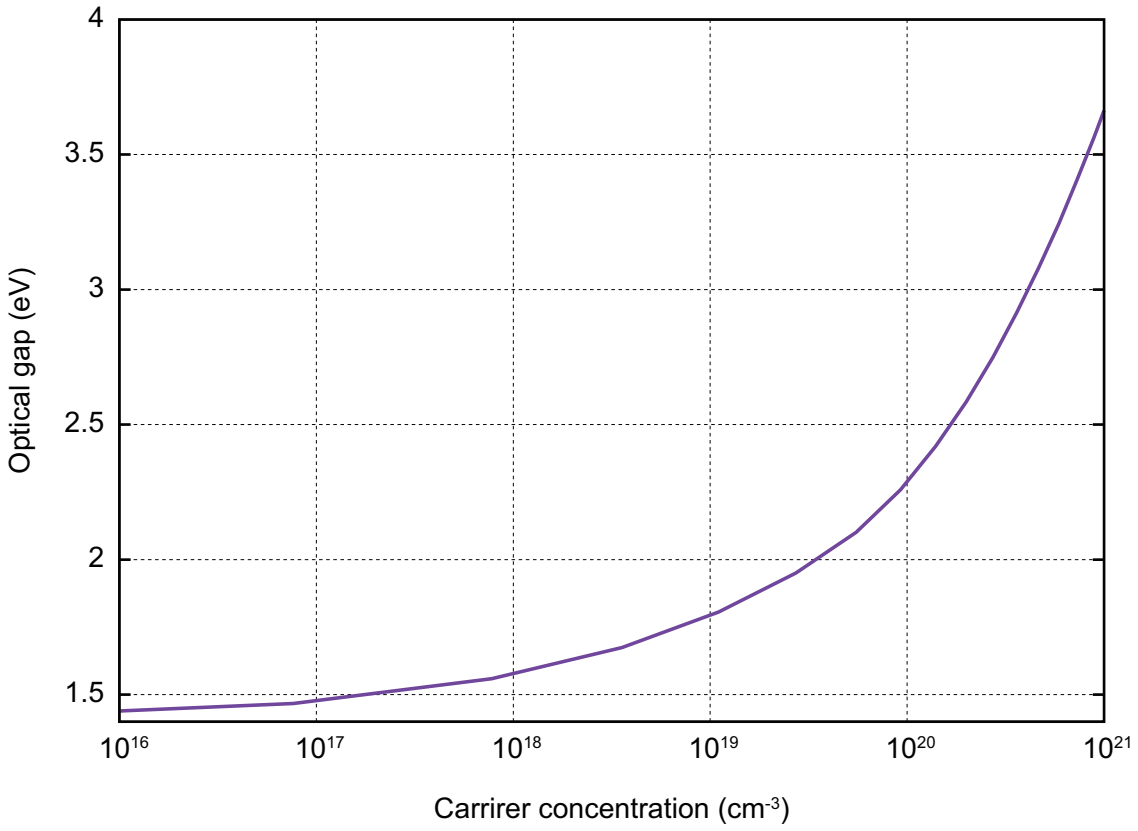

Figure S6: Optical gap as a function of the carrier-electron concentration for the ordered $ZnSnN_2$ calculated from the band structure and DOS using HSE06. The band dispersions of the valence and conduction bands were explicitly considered to evaluate the minimum vertical transition energy at each value of the carrier-electron concentration (see Ref. [10]).

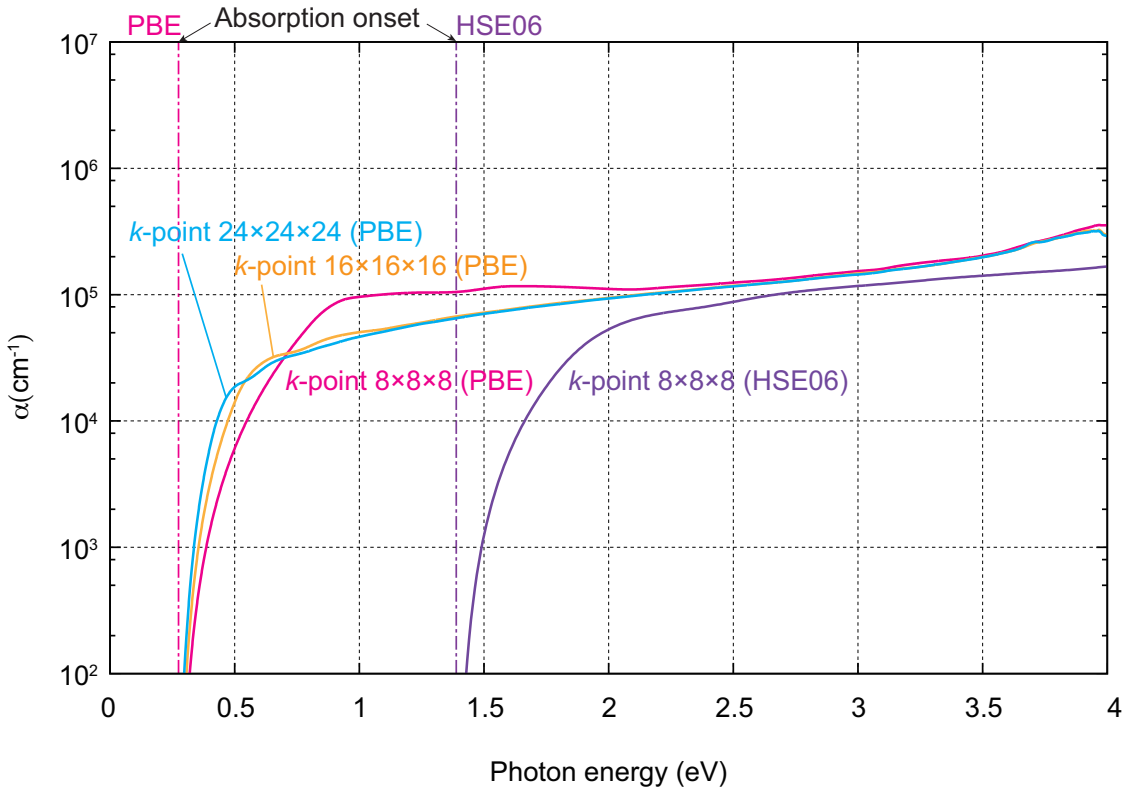

Figure S7: Absorption spectra for ordered $ZnSnN_2$ calculated using HSE06 and PBE-GGA [11] with the 16-atom unit cell. The calculated band gaps with 8×8×8 *k*-point sampling are also shown by dashed-dotted lines. The HSE06 calculation was performed with 8×8×8 *k*-point sampling, whereas the PBE-GGA ones with 8×8×8, 16×16×16, and 24×24×24 *k*-point sampling; the lesser *k*-point set for the former is due to much higher computational cost of the HSE06 hybrid functional. The HSE06 result with 8×8×8 *k*-point sampling shows a sharp initial rise of the absorption spectrum near the band gap of 1.4 eV. Note, however, as inferred from the PBE results showing non-negligible *k*-point sampling dependencies, the HSE06 absorption coefficient would be increased near the onset when using well converged *k*-point sampling.

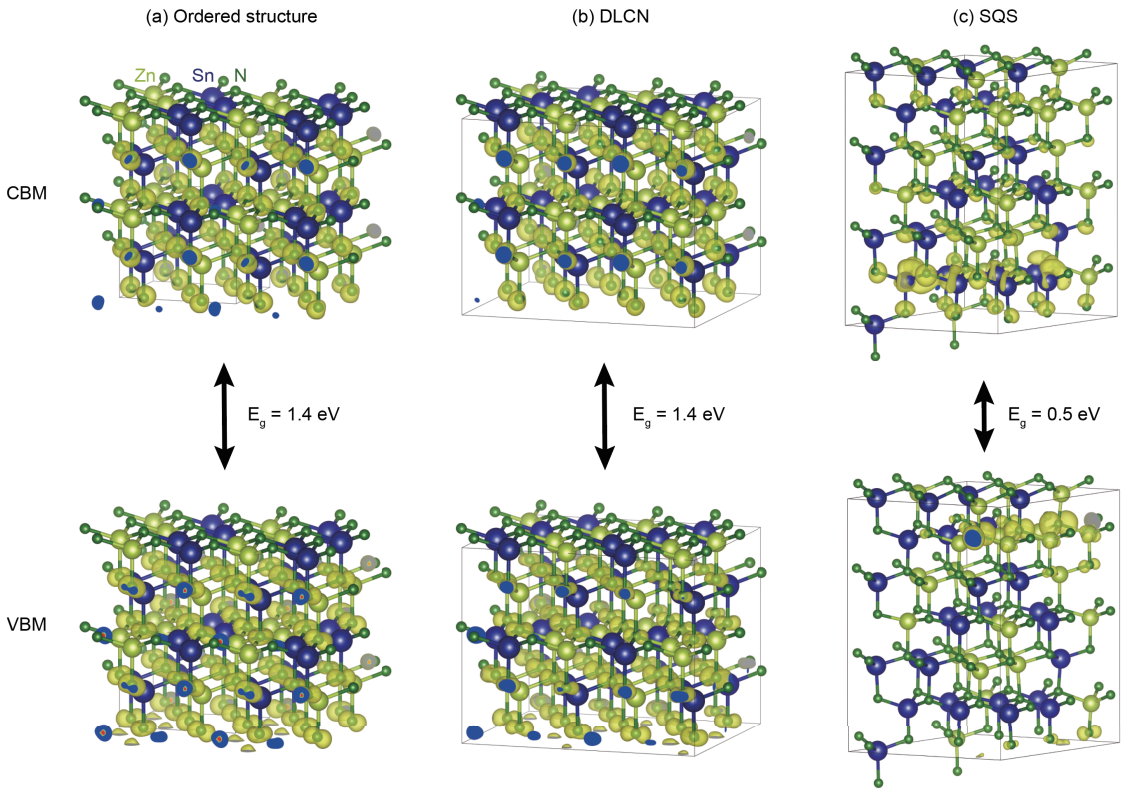

Figure S8: Isosurfaces of the squared wave functions at the VBM and CBM in (a) ordered, (b) DLCN, and (c) SQS $ZnSnN_2$. The band gap values are also shown. There is no significant difference in the distribution of the wave functions between the ordered and DLCN models. In contrast, the wave function at the VBM in the SQS model is largely localized at the N site with higher Zn coordination numbers, similarly to the Zn_{Sn} antisite defect (see the main text), while that at the CBM is localized at the Sn site. The VESTA code [3] was used for visualization.

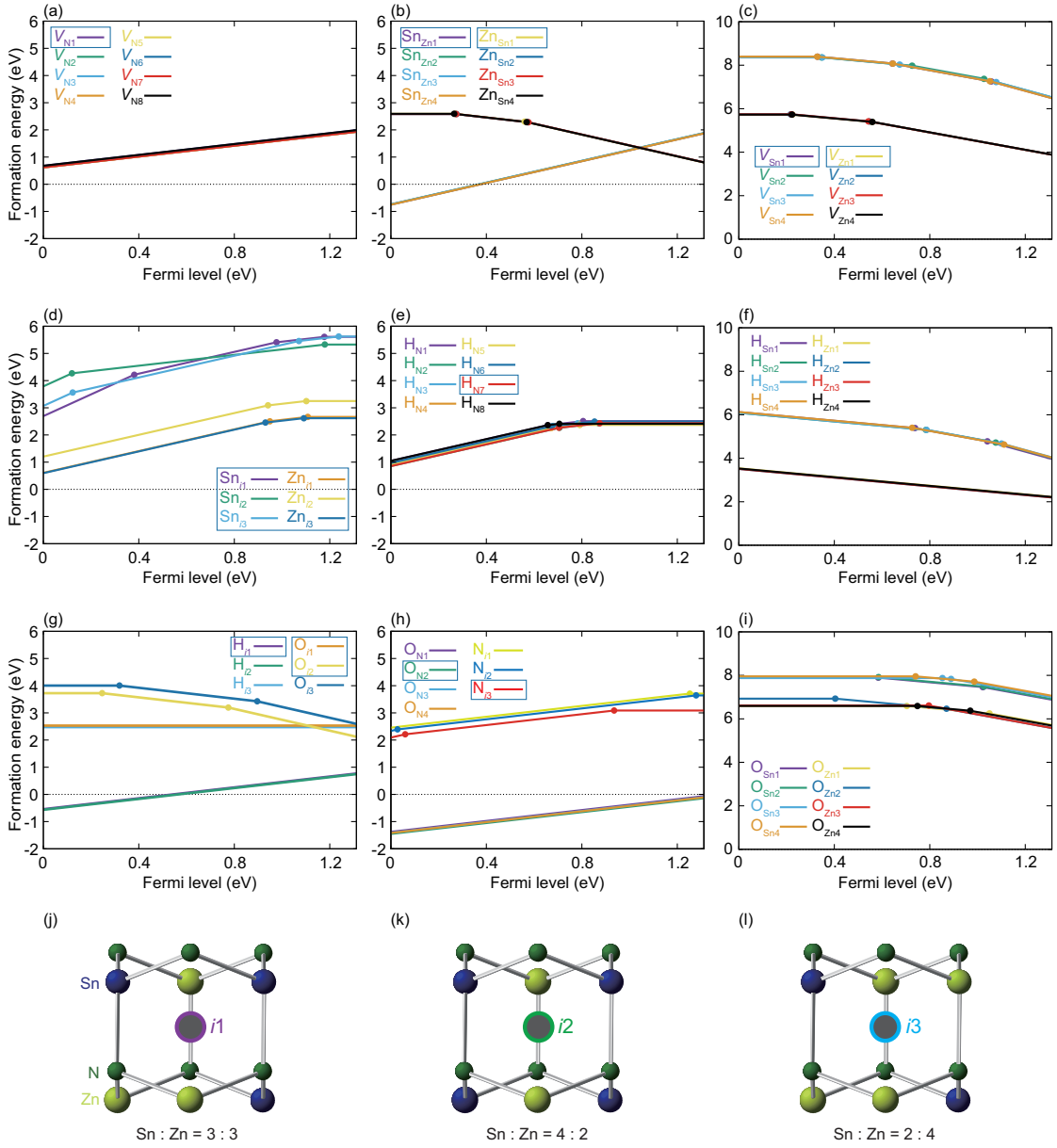

Figure S9: (a–i) Site dependencies of the defect-formation energies in the DLCN model shown in Figure 1(b) in the main text as a function of the Fermi level and (j, k, l) local structures near these interstitial sites considered. Here, PBEsol-GGA was used in conjunction with the 2×2×2 Monkhorst-Pack (MP) k-point mesh. Errors associated with the finite supercell size were corrected for all the defects using the extended FNV correction scheme. One can see that site dependences are negligibly small, especially for defects with lower formation energies. Relatively large variations are seen in interstitial-type defects, presumably because of the difference in neighboring cation configurations as shown in (j, k, l); the difference in the neighboring Sn:Zn ratios results in different electrostatic effects on the interstitial-type defects. H_X and O_X sites (X= Zn, Sn) are not considered in HSE06 calculations because their energies are much higher than those of H_i and O_N. Configurations enclosed in squares were adopted for the HSE06 calculations in the main text. Spin polarization was not considered here in order to reduce the computational costs.

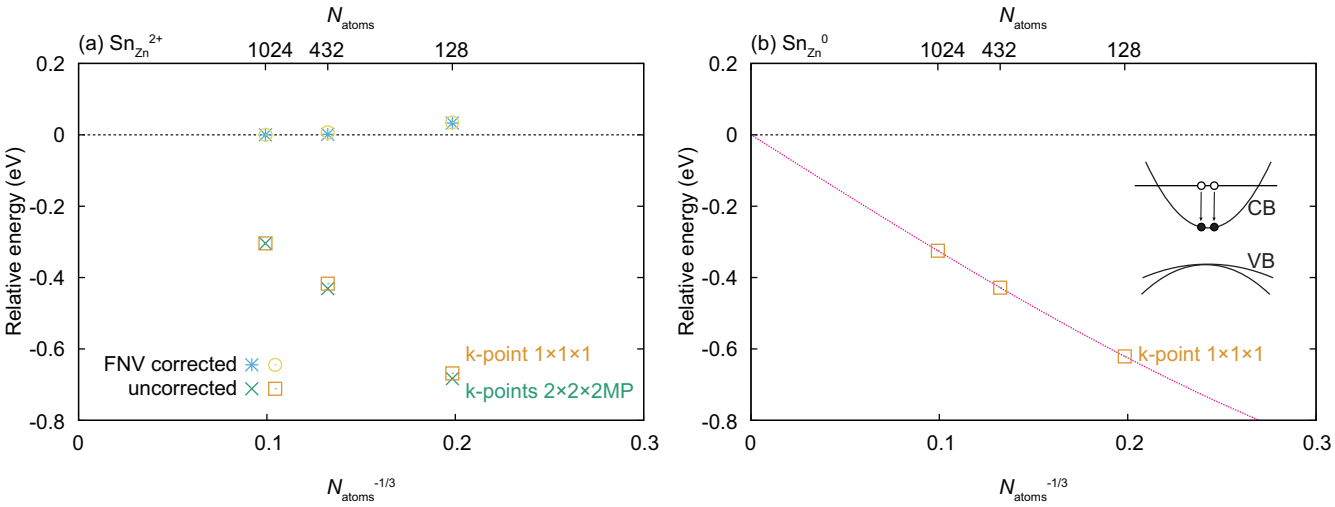

Figure S10: Formation energies of (a) Sn_{Zn}^{2+} and (b) Sn_{Zn}^{0} in the ordered $ZnSnN_2$ as a function of the supercell size using PBEsol-GGA. N_{atom} is the number of atoms in the supercell. In the case of Sn_{Zn}^{2+}, corrected formation energies using the extended FNV method are also shown. The energy zero is set at the corrected energy calculated using the largest 1024-atom supercell. The estimated error in the 128-atom supercell is 0.72 eV, but it is reduced to less than 0.05 eV when the FNV corrections are applied. In the case of Sn_{Zn}^{0}, the supercells contain a doubly occupied hydrogenic donor state whose electrons are released from a defect state as shown by the schematic illustration. One can see a large cell size dependence, although the charge state is neutral. This is mostly attributed to the interaction between the doubly ionized Sn_{Zn}, its periodic images, and hydrogenic donor electrons that spread throughout the supercell and behave like the background charge. See Refs. [12, 10] for more details.

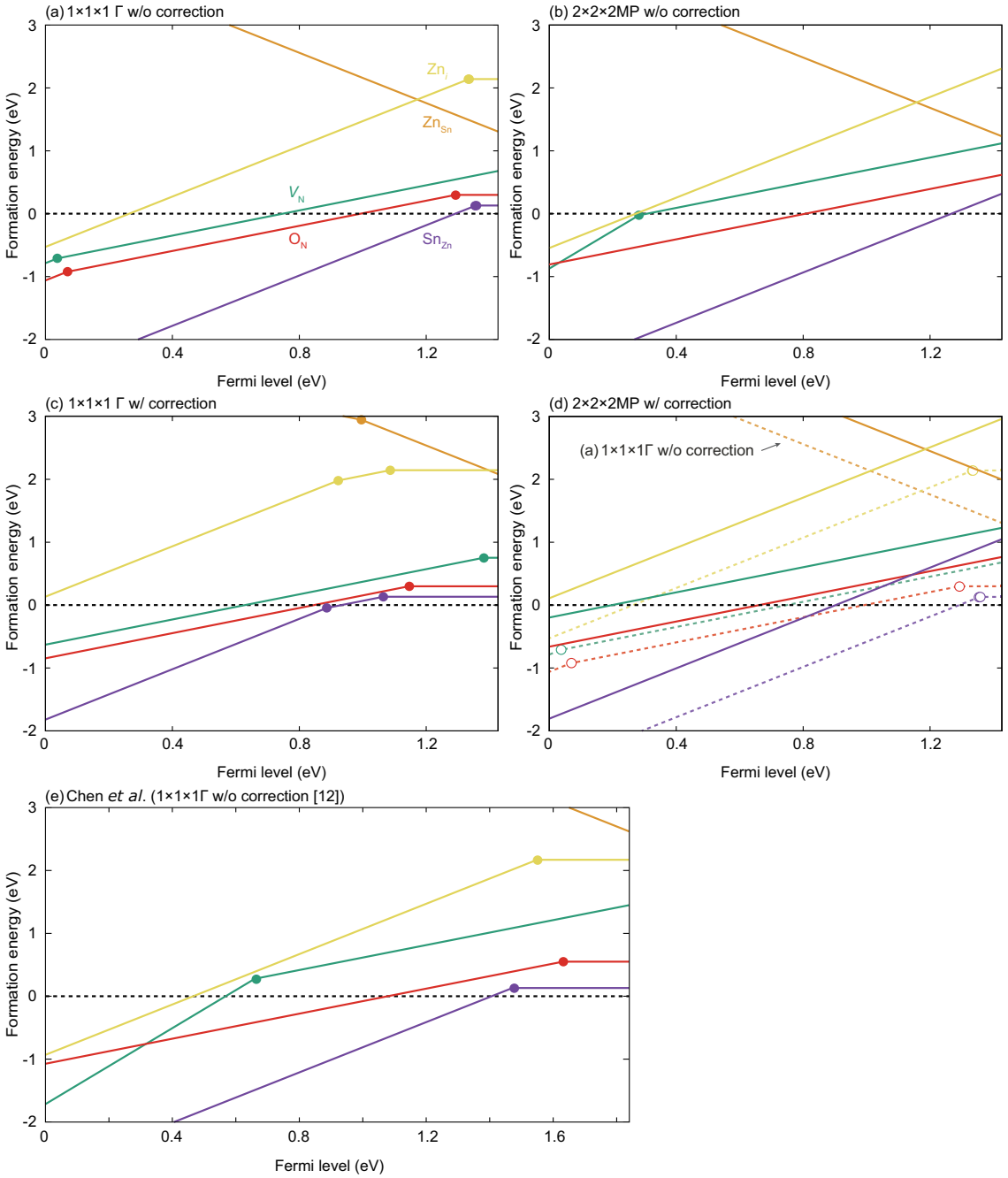

Figure S11: Defect-formation energies as a function of the Fermi level in the ordered $ZnSnN_2$ (a, b) without (w/o) and (c, d) with (w/) finite cell size corrections. (a, c) The Γ-point and (b, d) the 2×2×2 MP *k*-point mesh were used for reciprocal space sampling. The cell size corrections were performed using the extended FNV correction scheme. One can see the importance of the cell-size corrections and *k*-point sampling. (e) The formation energies calculated by Chen et al. reproduced from Ref. [13]. They used the same calculation condition with (a), namely no finite-cell size corrections and Γ-point only *k*-point sampling, but the mixing parameter of HSE was increased from 0.25 to 0.31, resulting in a larger band gap.

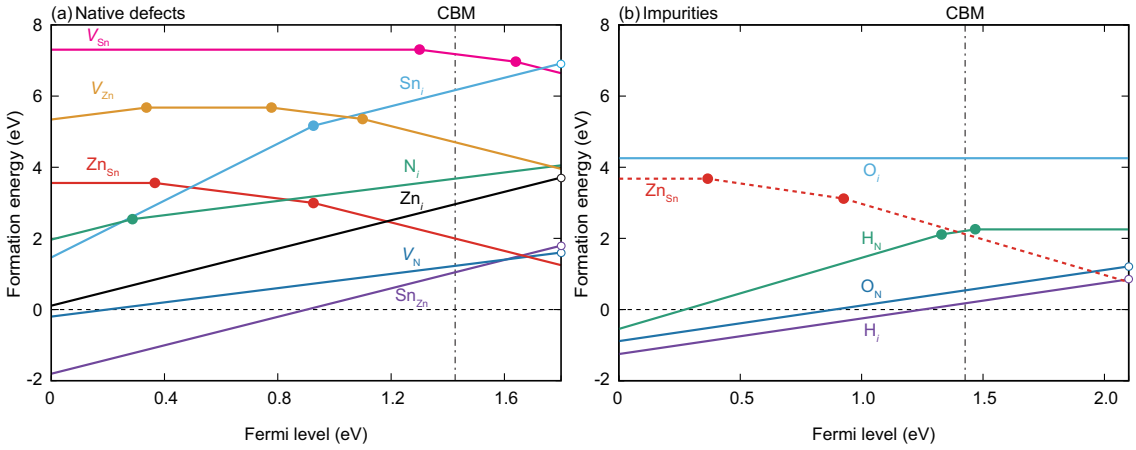

Figure S12: Formation energies of (a) native defects and (b) impurities in the ordered $ZnSnN_2$ as a function of the Fermi level. In (b), the formation energy of the dominant acceptor Zn_{Sn} among the native defects is also shown for comparison. The upper limit of the Fermi level is extended up to (a) 1.8 eV and (b) 2.1 eV with respect to the VBM, respectively, so that the intersections between the formation energies of the dominant donors and acceptors are visible. The transition levels above the CBM are calculated properly when the *k*-point mesh used for the defect calculations does not sample the CBM. In this study, we used the 2×2×2 MP *k*-point mesh, in which the lowest unoccupied state in the perfect supercell is located at 2.34 eV above the VBM (see Ref. [10] for details).

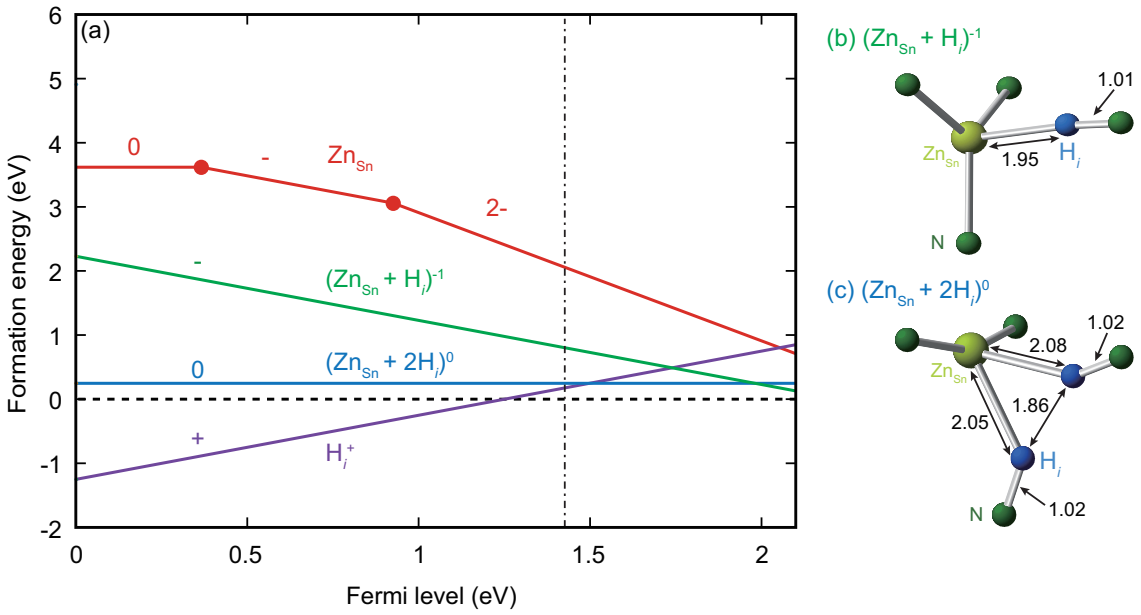

Figure S13: (a) Formation energies of H_i and Zn_{Sn} and their complex defects $(Zn_{Sn} + H_i)^-$ and $(Zn_{Sn} + 2H_i)^0$ calculated using HSE06. Relaxed atomic structures of $(Zn_{Sn} + H_i)^-$ and $(Zn_{Sn} + 2H_i)^0$ are shown in (b) and (c), respectively. The distances between atoms indicated by arrows in (b) and (c) are shown in Å. Note that only one configuration for each complex defect is considered. Complexing with hydrogen is exothermic and drastically decreases the formation energy of acceptor Zn_{Sn}. See main text for details.

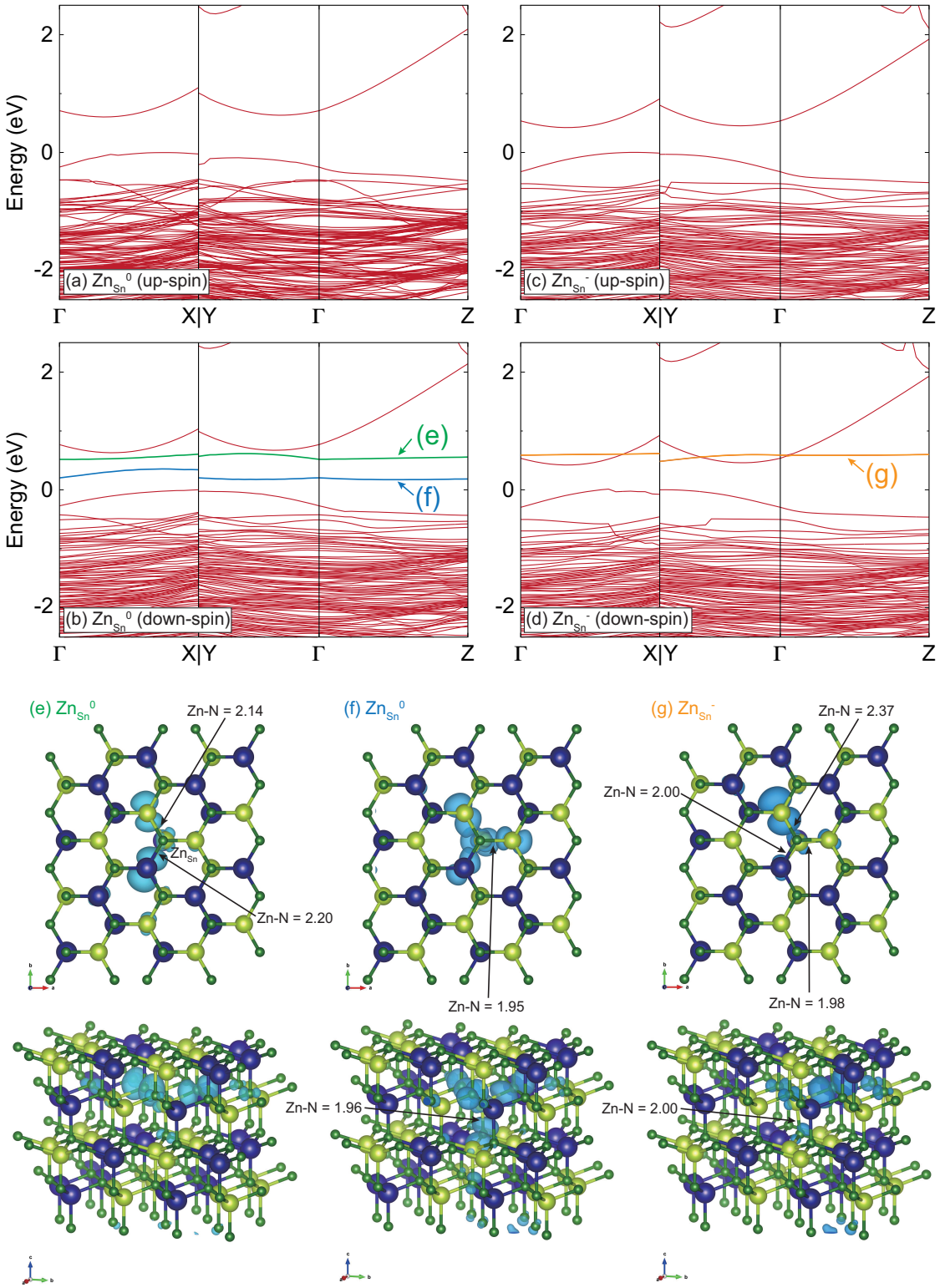

Figure S14: (a–d) Band structures for the up-spin and down-spin channels of Zn^{0}_{Sn} and Zn^{-}_{Sn} in the 128-atom supercell of the ordered model. (e–g) Squared wave functions of the bands highlighted in Figures (b) and (d), indicating localized defect states. The distances of Zn_{Sn}-N are indicated by arrows in Å. Note that the Zn^{2-}_{Sn}-N distances are 2.04–2.07 Å. As discussed in the main text, two holes in the Zn^{0}_{Sn} model are located in the down-spin channel within the band gap, while one hole in the Zn^{-}_{Sn} model is in the same channel but slightly above the CBM. The deep levels exist as hole polaronic states captured by the neighboring N atoms with accompanying outward relaxations as seen in (e–g).

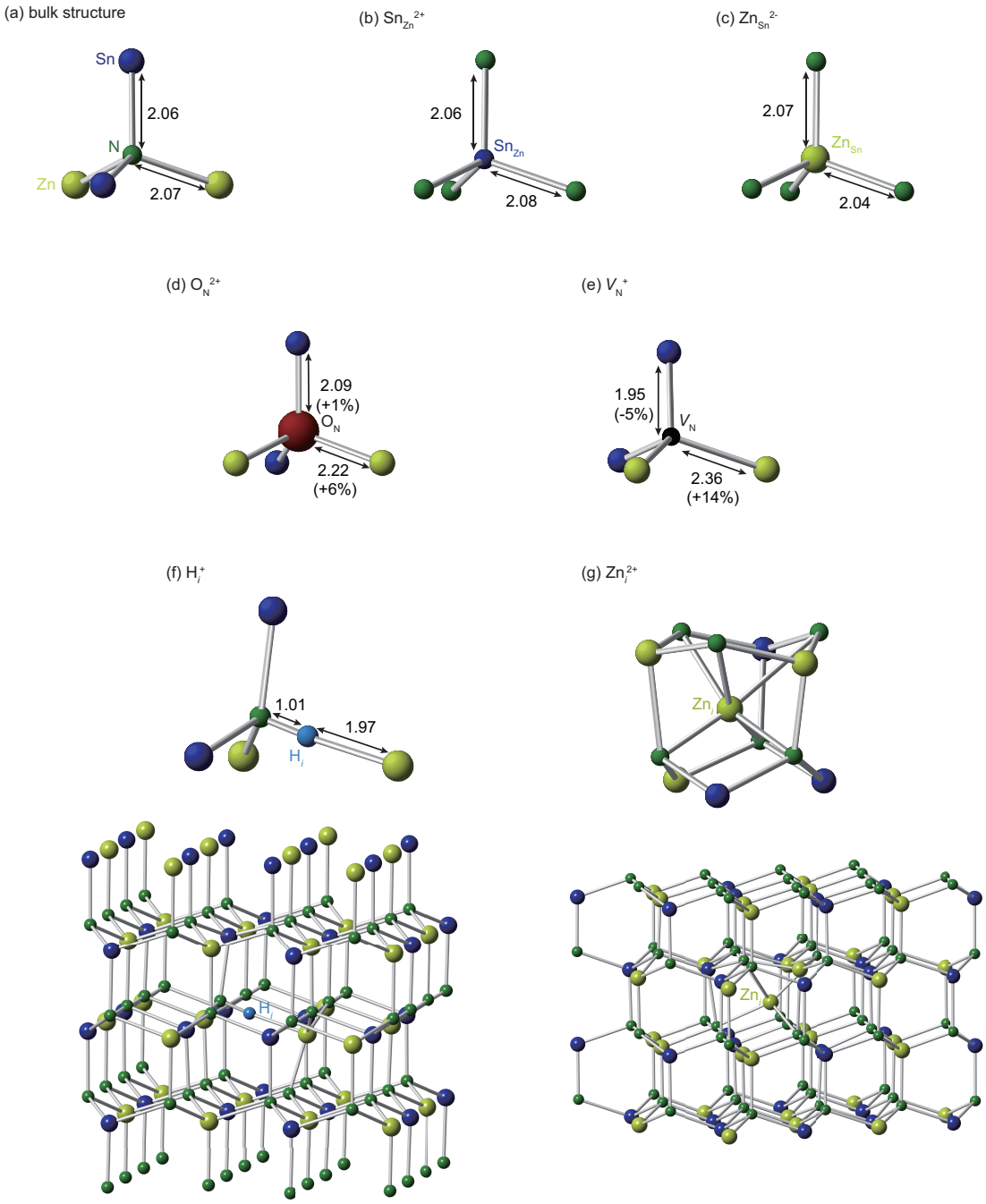

Figure S15: Local defect structures in the ordered $ZnSnN_2$. The distances between atoms are shown in Å. For comparison, the tetrahedral configuration around an N atom in the ordered $ZnSnN_2$ is shown in (a). Sn_{Zn}^{2+}, Zn_{Sn}^{2-}, and O_N^+ in (b), (c), and (d), respectively, show relatively small displacements of coordinating atoms probably because of similar ionic radii between Zn and Sn and between N and O. V_N^+ in (e) shows inward relaxations of Sn atoms with an occupied Sn-Sn bond and outward relaxations of Zn atoms. H_i^+ in (f) is located in between N and Zn with forming a strong N-H bond. Zn_i^{2+} in (g) is slightly off-centered from the octahedral site. Larger areas are also depicted for (f) H_i^+ and (g) Zn_i^{2+}.

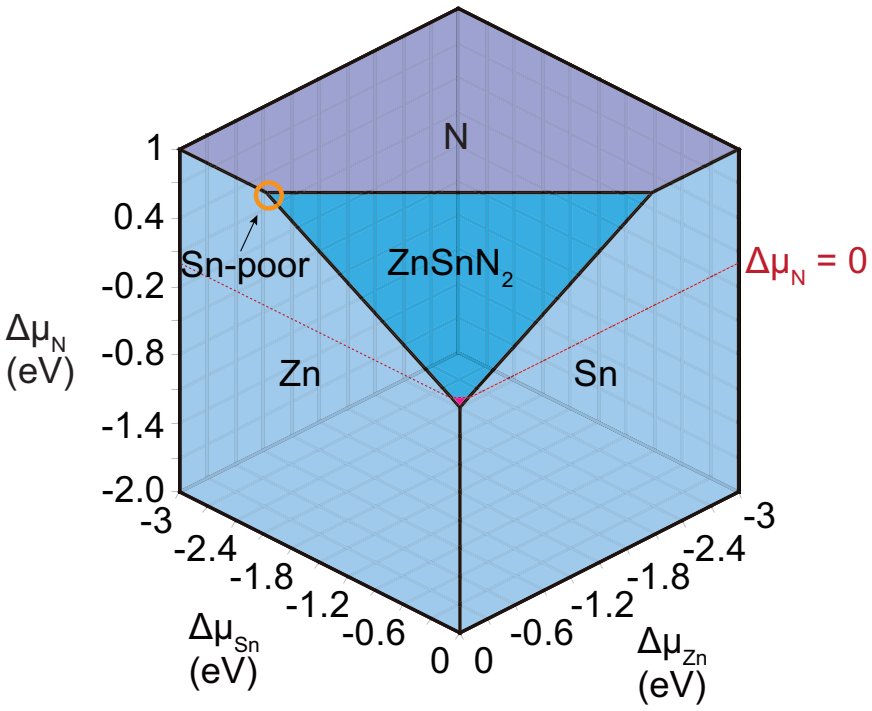

Figure S16: Chemical potential diagram that shows the condition considered to achieve the low carrier-electron concentration in $ZnSnN_2$. As discussed in the main text, the nitrogen chemical potential $\Delta\mu_N$ is increased by 1 eV from the energy of the N_2 molecule per atom. The equilibrium point used for the calculations in Figure 3 in the main text is designated by an open circle, corresponding to the Sn-poor (Zn-rich) condition.

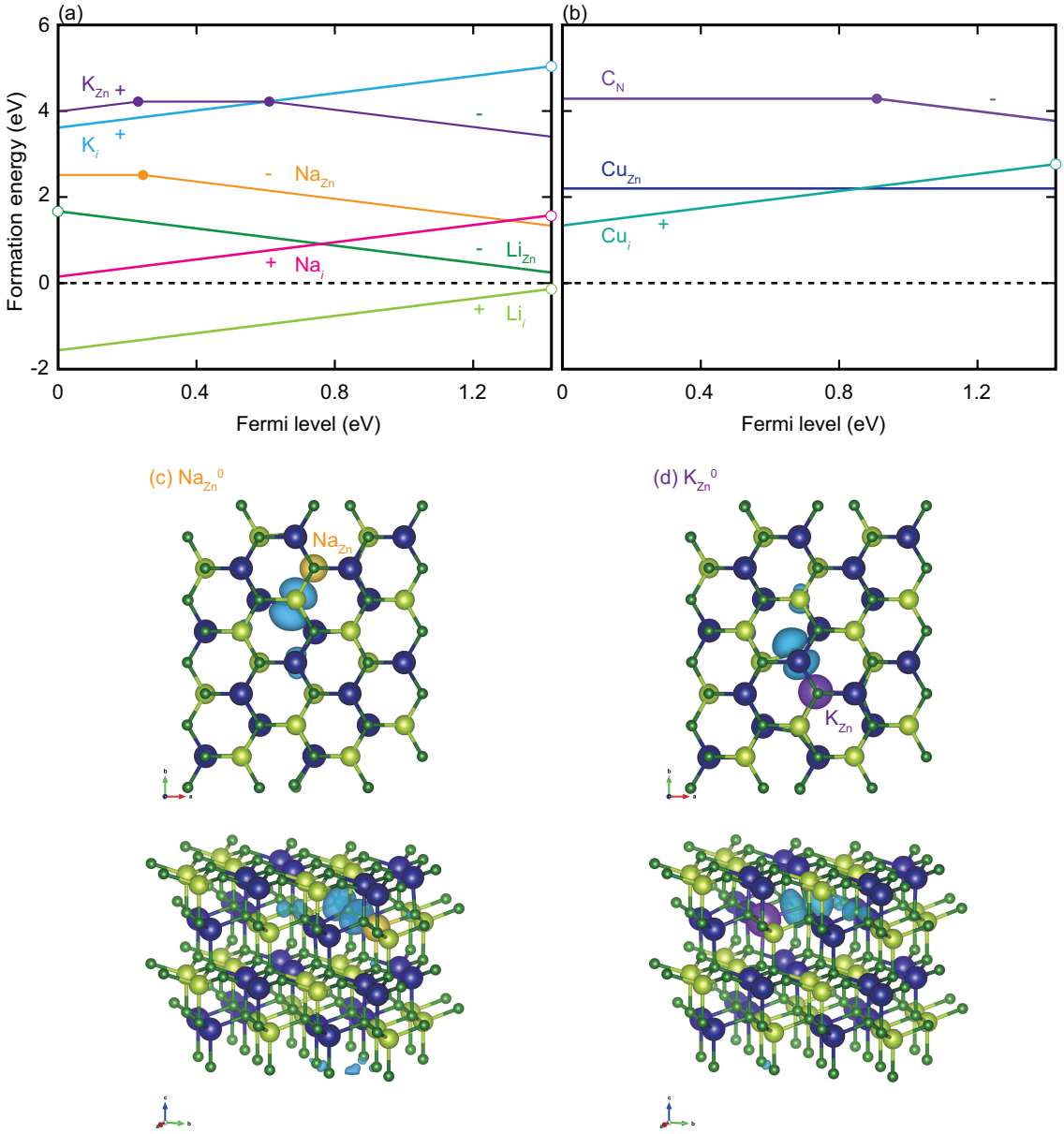

Figure S17: Formation energies of substitutional and interstitial (a) Li, Na, and K, and (b) Cu and C considered as acceptor dopants in the ordered $ZnSnN_2$ at the Sn-poor (Zn-rich) condition in Figure S16. (c, d) Squared wave functions of the hole trapping states in Na_{Zn}^0, and K_{Zn}^0 models. All the monovalent cations (Li, Na, K, and Cu) favor the interstitial site in the *p*-type regime, and Cu_{Zn} and C_N show extremely deep acceptor levels, indicating difficulty of *p*-type doping with these dopants. It is also noteworthy in view of electronic structure that Na_{Zn} and K_{Zn} show similar polaronic behaviors to Zn_{Sn}; they exist as hole polarons locating at the N sites near the defects, as seen in (c) and (d). In the cases of C_N and Cu_{Zn}, on the other hand, a hole is localized at the C-*p* state and Cu-3*d* state, respectively.

[1] Y. Hinuma, G. Pizzi, Y. Kumagai, F. Oba, and I. Tanaka, "Band structure diagram paths based on crystallography," Computational Materials Science **128**, 140 (2017).

[2] Y. Hinuma, T. Hatakeyama, Y. Kumagai, L. A. Burton, H. Sato, Y. Muraba, S. Iimura, H. Hiramatsu, I. Tanaka, H. Hosono, and F. Oba, "Discovery of earth-abundant nitride semiconductors by computational screening and high-pressure synthesis," Nature Communications **7**, 11962 (2016).

[3] K. Momma and F. Izumi, "VESTA 3 for three-dimensional visualization of crystal, volumetric and morphology data," J. Appl. Cryst. **41**, 653 (2008).

[4] J. Li, K. B. Nam, M. L. Nakarmi, J. Y. Lin, H. X. Jiang, P. Carrier, and S.-H. Wei, "Band structure and fundamental optical transitions in wurtzite AlN," Applied Physics Letters **83**, 5163 (2003).

[5] H. P. Maruska and J. J. Tietjen, "The Preparation and Properties of Vapor-Deposited Single-Crystal GaN," Applied Physics Letters **15**, 327 (1969).

[6] J. Wu, W. Walukiewicz, S. X. Li, R. Armitage, J. C. Ho, E. R. Weber, E. E. Haller, H. Lu, W. J. Schaff, A. Barcz, and R. Jakiela, "Effects of electron concentration on the optical absorption edge of InN," Applied Physics Letters **84**, 2805 (2004).

[7] R. Deng, B. D. Ozsdolay, P. Y. Zheng, S. V. Khare, and D. Gall, "Optical and transport measurement and first-principles determination of the ScN band gap," Phys. Rev. B **91**, 045104 (2015).

[8] M. Futsuhara, K. Yoshioka, and O. Takai, "Structural, electrical and optical properties of zinc nitride thin films prepared by reactive RF magnetron sputtering," Thin Solid Films **322**, 274 (1998).

[9] A. Seko, Y. Koyama, and I. Tanaka, "Cluster expansion method for multicomponent systems based on optimal selection of structures for density-functional theory calculations," Phys. Rev. B **80**, 165122 (2009).

[10] Y. Kumagai, K. Harada, H. Akamatsu, K. Matsuzaki, and F. Oba, "Carrier-Induced Band-Gap Variation and Point Defects in Zn_3N_2 from First Principles," Phys. Rev. Applied **8**, 014015 (2017).

[11] J. P. Perdew, K. Burke, and M. Ernzerhof, "Generalized gradient approximation made simple," Phys. Rev. Lett. **77**, 3865 (1996).

[12] F. Oba, A. Togo, I. Tanaka, J. Paier, and G. Kresse, "Defect energetics in ZnO: A hybrid hartree-fock density functional study," Phys. Rev. B **77**, 245202 (2008).

[13] S. Chen, P. Narang, H. A. Atwater, and L.-W. Wang, "Phase stability and defect physics of a ternary ZnSnN2 semiconductor: First principles insights," Advanced Materials **26**, 311 (2014).